

## RESEARCH ARTICLE

10.1002/2016JD025317

## Key Points:

- Radar observations indicate the occurrence of deep convection at the major axis tips in elliptical eyewall tropical cyclones
- Nondivergent barotropic model and slab boundary layer model are used to understand this phenomenon
- The strong updrafts at the edges of the major axes are from the shock-like boundary layer radial wind structure

## Correspondence to:

Y.-T. Yang,  
d97229001@ntu.edu.tw

## Citation:

Kuo, H.-C., W.-Y. Cheng, Y.-T. Yang, E. A. Hendricks, and M. S. Peng (2016), Deep convection in elliptical and polygonal eyewalls of tropical cyclones, *J. Geophys. Res. Atmos.*, 121, 14,456–14,468, doi:10.1002/2016JD025317.

Received 7 MAY 2016

Accepted 1 DEC 2016

Accepted article online 6 DEC 2016

Published online 29 DEC 2016

## Deep convection in elliptical and polygonal eyewalls of tropical cyclones

Hung-Chi Kuo<sup>1</sup> , Wei-Yi Cheng<sup>2</sup>, Yi-Ting Yang<sup>3</sup> , Eric A. Hendricks<sup>4</sup>, and Melinda S. Peng<sup>5</sup>
<sup>1</sup>Department of Atmospheric Sciences, National Taiwan University, Taipei, Taiwan, <sup>2</sup>Department of Atmospheric Sciences, University of Washington, Seattle, Washington, USA, <sup>3</sup>Taida Institute for Mathematical Sciences, National Taiwan University, Taipei, Taiwan, <sup>4</sup>Department of Meteorology, U.S. Naval Postgraduate School, Monterey, California, USA, <sup>5</sup>Marine Meteorology Division, Naval Research Laboratory, Monterey, California, USA

**Abstract** In observations, tropical cyclones with cyclonically rotating elliptical eyewalls are often characterized by wave number 2 (WN2) deep convection located at the edge of the major axis. A simple modeling framework is used to understand this phenomenon, where a nondivergent barotropic model (NBM) is employed to represent the elliptical vortex in the free atmosphere, and an asymmetric slab boundary layer (SBL) model is used to simulate the frictional boundary layer (BL) underneath the free atmosphere. The interaction is one way in that the overlying cyclonic flow drives the BL, but the BL pumping does not feed back to the overlying flow. The nonlinear-balanced pressure field from the NBM drives the winds in the SBL model, which then causes BL convergence and pumping near the eyewall. The strong updrafts at the edge of the major axis for the elliptic vortex in the BL are induced by the larger convergent radial wind from the asymmetric distribution of the pressure fields of the free atmosphere with noncircular vortex. The large radial inflow maintains the supergradient wind at the edge of the elliptical vortex. The results emphasize the cyclonic rotation of the WN2 feature of strong updrafts at the top of the BL from the local shock-like BL radial wind structure. Similar radial profiles and strong BL top updrafts occur at the edges of higher-order polygonal eyewalls with the magnitude of the peak updraft decreasing as the wave number structure of the vortex increases.

## 1. Introduction

The organization and structure of a tropical cyclone (TC) is mainly controlled by the convective process. *Ooyama* [1969], using a symmetric vortex, suggested that the boundary layer (BL) convergence can contribute to the organization of convection in the inner core of a TC. *Powell* [1982] studied the isotach distribution in the BL of Hurricane Frederic (1979) and proposed a relationship between the BL wind, the convection, and the motion of the hurricane. The BL tangential winds were in general strong on the right-front quadrant of the TC. *Shapiro* [1983] used a slab boundary layer (SBL) model of constant depth to study the wave number 1 (WN1) asymmetric convection under a translating hurricane. Large convergence often occurred in the right-front quadrant of the storm motion in cases with large translation speed. In the convergent region, the tangential wind in the BL is supergradient within  $r < r_{\max}$  and is subgradient in  $r > r_{\max}$ , where  $r_{\max}$  is the radius of maximum wind (RMW). The modeling results were in general agreement with the observational study of *Powell* [1982].

*Williams et al.* [2013] used an axisymmetric SBL model to interpret aircraft observations from Hurricane Hugo (1989). Their results indicate that in Category 3 hurricanes (tangential wind is approximately  $55 \text{ m s}^{-1}$ ), the BL inflow decreases from approximately  $22 \text{ m s}^{-1}$  to zero over a radial distance of a few kilometers (i.e., a shock-like structure). They demonstrated that the nonlinear advection of the radial momentum produces shock-like structures for the radial wind within the TC BL. This radial convergence can lead to updrafts exceeding  $22 \text{ m s}^{-1}$  at a height of 1000 m, which is important to initiate convection in TCs. In addition, the shock-like structure in the BL has a strong impact on the tangential wind and vorticity. On the inner side of the shock, the tangential wind tendency is essentially zero, while on the outer side of the shock the tangential wind tendency is largely due to the strong radial inflow there. The result then is the development of a U-shaped tangential wind profile and large vorticity in a thin radial region. *Abarca et al.* [2015] suggested that shock-like structures are not found in the azimuthally averaged vortex BL. It is possible, however, that the shock-like structure may occur locally in the BL and not in the azimuthally averaged structure. Since the dynamical

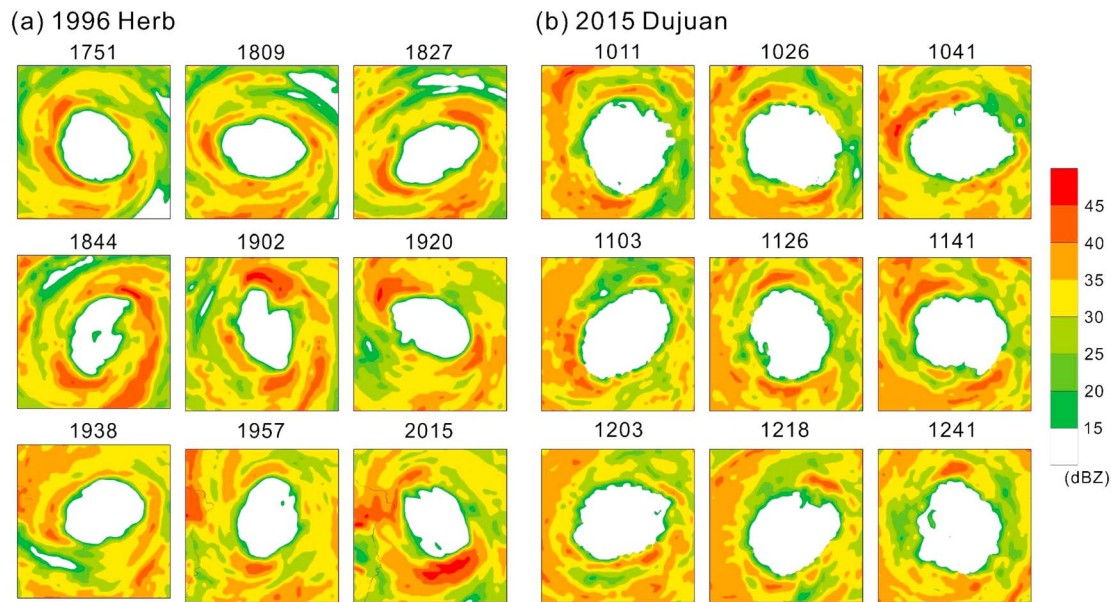


**Figure 1.** Radar reflectivity of (a) Typhoon Herb (1996) from 1751 LCT to 2015 LCT on 31 July 1996 and (b) Typhoon Dujan (2015) from 1011 LCT to 1241 LCT on 28 September 2015. The local time of observations is indicated on the top of each figure, which has domain of  $120 \text{ km} \times 120 \text{ km}$ .

mechanism for shock formation is the nonlinear advection term in the momentum equation, shocks may also occur locally (without the assumption of axisymmetry or the choice of a particular coordinate system).

Using a nonlinear, nondivergent barotropic model (NBM), Kuo *et al.* [1999] suggested that the vortex Rossby wave (VRW) dynamics [Montgomery and Kallenbach, 1997] causes the elliptical eye to rotate anticyclonically relative to the mean flow. This causes the elliptical eye to move more slowly relative to the mean flow. Following the pioneering work of Kelvin [Thomson, 1880], Kuo *et al.* [1999] proposed that the cyclonic rotation of asymmetric perturbations in polygonal eyewalls as the VRW follows with  $c = V_{\text{max}} (1 - 1/m)$ , where  $c$  is the wave phase speed,  $V_{\text{max}}$  is the vortex maximum wind, and  $m$  is the azimuthal wave number. Results using the NBM for the cyclonic rotation of elliptical vortex by Kuo *et al.* [1999] are in general agreement with the nonlinear theory of the Kirchhoff elliptical vortex [Lamb, 1932, p. 232].

Muramatsu [1986] used a land-based radar data for a 15 h period to study polygonal eyewalls in Typhoon Wynne (1980). The polygonal structures investigated included squares, pentagons, and hexagons. It was shown that pentagons and squares had rotation periods of approximately 42 min and 48 min, respectively. The rotation period decreased as the tangential wave number (WN) structure of the vortex increased. This is in general agreement with the modeling results of Kurihara and Bender [1982]. Itano and Hosoya [2013] studied the geometry of convection in the polygonal eye of Typhoon Sinlaku (2002). Their analysis revealed the dominance of WN2 and WN5 convective perturbations with angular velocities of approximately  $80^\circ \text{ h}^{-1}$  and  $130^\circ \text{ h}^{-1}$ , respectively, in Typhoon Sinlaku. The observations were also in general agreement with the linear theory of Kelvin [Thomson, 1880].

There is observational evidence that deep convection often occurs near the edges of the major axis of an elliptical eyewall. Examples include the Second Miyakojima Typhoon (1966) [Mitsuta and Yoshizumi, 1973, Figure 10], Hurricane Allen (1980) [Shapiro, 1983, Figure 10], Hurricane Elena (1985) [Corbosiero *et al.*, 2006, Figure 4a], and Hurricane Erin (2001) [Aberson *et al.*, 2006, Figure 3]. Figure 1 shows two examples of elliptical eyewall structures from the radar reflectivity observed for Typhoons Herb (1996) and Dujan (2015). Figure 1a is the same as Figure 2 from Kuo *et al.* [1999], except in color and in a smaller domain. Both have WN2 deep convective structures at the edges of the major axis that rotate cyclonically with the elliptical eye. In the case of Typhoon Dujan (2015), the rotation period of WN2 deep convection perturbation was approximately 150 min ( $144^\circ \text{ h}^{-1}$ ). The maximum wind, as estimated by Central Weather Bureau in Taiwan, was  $64 \text{ m s}^{-1}$  and the size was 46 km. Thus, the rotation speed was found to be approximately half the maximum tangential wind. The presence of deep convection at the edges of the cyclonically rotating major axis has also been

identified in numerical simulations. *Braun* [2002] used the Pennsylvania State University–National Center for Atmospheric Research fifth-generation Mesoscale Model with a horizontal resolution of 1.3 km on the finest nested mesh to simulate Hurricane Bob (1991). The distribution of radial flow, vertical motion, and precipitation were shown to be amplified by a WN2 asymmetry that rotates cyclonically around the center at about half the speed of the mean tangential winds, consistent with the linear theory of Kelvin.

This paper investigates the structure of BL pumping and convection in TCs with elliptical or other polygonal eyewalls. In particular, our emphasis is on the dynamics associated with the WN2 deep BL pumping and convection at the edges of the major axis of the eyewall. We use a nonlinear NBM combined with an asymmetric SBL model for our study. The NBM is a one-layer model designed to model the cyclonic rotation of the elliptical vortex in the quasi-inviscid free atmosphere above the BL, and the asymmetric SBL model is designed to represent the BL underneath the free atmosphere. The system is used to obtain a basic understanding of how the BL responds to an elliptical or polygonal vortex of the free atmosphere. The rest of the paper is organized as follows: section 2 describes the system and the model parameters, the results from the numerical experiments are presented and discussed in section 3, and a summary is given in section 4.

## 2. Model and Experiment Design

A simple modeling framework of NBM and an asymmetric SBL model is used in the study. The NBM on an  $f$  plane with horizontal diffusivity can be written as

$$\frac{\partial \zeta}{\partial t} + J(\psi, \zeta) = \nu \nabla^2 \zeta, \quad (1)$$

$$\zeta = \nabla^2 \psi, \quad (2)$$

where  $J(\psi, \zeta)$  denotes the Jacobian of the stream function  $\psi$  and the relative vorticity  $\zeta$ . The balanced pressure field in NBM can be solved from the nonlinear balance condition with the known stream function field:

$$\frac{1}{\rho} \nabla^2 p = f \nabla^2 \psi + 2 \left[ \frac{\partial^2 \psi}{\partial x^2} \frac{\partial^2 \psi}{\partial y^2} - \left( \frac{\partial^2 \psi}{\partial x \partial y} \right)^2 \right]. \quad (3)$$

In order to address the asymmetric dynamics in BL, we write the governing SBL equations in Cartesian coordinates,

$$\frac{\partial u}{\partial t} = -u \frac{\partial u}{\partial x} - v \frac{\partial u}{\partial y} - w^- \left( \frac{u_r - u}{h} \right) + f \left( v - \frac{1}{\rho f} \frac{\partial p}{\partial x} \right) - C_D U \frac{u}{h} + K \nabla^2 u, \quad (4)$$

$$\frac{\partial v}{\partial t} = -u \frac{\partial v}{\partial x} - v \frac{\partial v}{\partial y} - w^- \left( \frac{v_r - v}{h} \right) - f \left( u - \frac{1}{\rho f} \frac{\partial p}{\partial y} \right) - C_D U \frac{v}{h} + K \nabla^2 v, \quad (5)$$

$$w = -h \left( \frac{\partial u}{\partial x} + \frac{\partial v}{\partial y} \right), \quad (6)$$

where  $x$  is the distance in the zonal direction,  $y$  is the distance in the meridional direction,  $u$  is the zonal velocity,  $v$  is the meridional velocity,  $w$  is the vertical motion at the top of the BL,  $w^- = \frac{1}{2}(|w| - w)$ ,  $p$  is the balanced pressure field,  $u_r = -\frac{\partial \psi}{\partial y}$  and  $v_r = \frac{\partial \psi}{\partial x}$  are the rotational winds from the NBM,  $\rho = 1.13 \text{ kg m}^{-3}$  is the density,  $K$  is the diffusivity,  $C_D$  is the drag coefficient,  $h$  is the constant depth of SBL, and  $f = 5 \times 10^{-5} \text{ s}^{-1}$  is the Coriolis parameter. *Powell et al.* [2003] found that the wind speed  $U$  for the drag coefficient is about 0.78 times the surface wind in general. We use  $U = 0.78(u^2 + v^2)^{1/2}$  in our SBL model, the same as in *Williams et al.* [2013]. The drag coefficient  $C_D$  formula follows *Powell et al.* [2003],

$$C_D = 10^{-3} \begin{cases} 2.70/U + 0.142 + 0.0764 U & \text{if } U \leq 25 \\ 2.16 + 0.5406 \left[ 1 - \exp\left(-\frac{U-25}{7.5}\right) \right] & \text{if } U \geq 25. \end{cases} \quad (7)$$

We have also used a  $C_D$  profile that does not decrease with increasing wind speeds in a vortex experiment with a maximum wind of  $60 \text{ m s}^{-1}$ . The BL pumping in our model does not appear to be sensitive to the choice of the  $C_D$  (not shown).

*Williams et al.* [2013] conducted a series of sensitivity tests of  $h$  and  $K$  in the SBL. They found that when reaching a steady state, a deeper  $h$  produces a stronger BL pumping, with the maximum pumping occurring at a larger radius and a larger  $K$  generating a broader shock-like structure and a smaller maximum pumping value. In the present work, since we are focusing on the dynamics of the asymmetric shock-like structure formation, we chose  $K = 1500 \text{ m}^2 \text{ s}^{-1}$ , as in *Zhang and Montgomery* [2012], and  $h = 1000 \text{ m}$ , following the work of *Williams et al.* [2013].

Equations (1)–(7) constitute a closed system with seven variables of  $C_D$ ,  $u$ ,  $v$ ,  $w$ ,  $p$ ,  $\psi$ , and  $\zeta$ . The system can be time integrated with the NBM to get the vorticity field and the rotational wind in the free atmosphere. The nonlinear balance equation is solved to obtain the pressure field. The pressure field and the rotational wind are then used to drive the SBL model and compute the BL pumping  $w$ . Equations (4) and (5) indicate that SBL model is influenced by the free atmosphere dynamics from the downward-only vertical momentum flux associated with the  $w^-$  terms and the pressure gradient force term.

Our model calculations are performed on a doubly periodic  $f$  plane. The discretization of both models is based on the Fourier pseudospectral method, with  $768 \times 768$  equally spaced collocation points on a  $300 \times 300 \text{ km}$  domain. The model was run with a dealiased calculation of quadratic nonlinear terms with  $256 \times 256$  Fourier modes. A fourth-order Runge-Kutta method with a 3 s time step was used for the time integration. The diffusion coefficient in the NBM was chosen to be  $\nu = 6.5 \text{ m}^2 \text{ s}^{-1}$ . For the  $300 \times 300 \text{ km}$  domain this value of  $\nu$  gives an  $e$ -folding damping time of 1.5 h for all modes having total wave number of 256 and a damping time of 5.9 h for modes having total wave number of 128.

We applied the Lanczos filter [Duchon, 1979] in each time step to the wind field in spectral space to mitigate the Gibbs oscillation. The Lanczos filter was used in *Kuo and Cheng* [1999] for their spectral convection model to filter the high-frequency acoustic modes. For a given physical field  $q$  in an  $N_x \times N_y$  collocation point domain, Fourier coefficients of wave numbers  $k$  and  $l$  are defined by

$$\hat{q}_{k,l} = \sum_{n=0, m=0}^{n=N_x, m=N_y} q(n, m) \times \exp \left[ -2\pi i \left( \frac{kn}{N_x} + \frac{lm}{N_y} \right) \right]. \quad (8)$$

Then we can apply a simple weighting function to  $\hat{q}_{k,l}$

$$\tilde{q}_{k,l} = \hat{q}_{k,l} \times \frac{\sin(k\pi/N_x)}{k\pi/N_x} \times \frac{\sin(l\pi/N_y)}{l\pi/N_y}, \quad (9)$$

where  $\tilde{q}_{k,l}$  is the filtered Fourier coefficient. Thus, we can smoothly reduce the high wave number signals since  $\lim_{x \rightarrow \pi} \frac{\sin x}{x} = 0$  while not losing much information of low wave numbers since  $\lim_{x \rightarrow 0} \frac{\sin x}{x} = 1$ .

We used the same Category 3 TC case as in *Williams et al.* [2013], and the simulation yields a very similar BL structure (not shown). Our model, however, produced a BL pumping which is approximately 75% in magnitude of the *Williams et al.* [2013], possibly due to the use of the Lanczos filter and the slightly coarser resolution in our model.

We follow *Kuo et al.* [1999] for the initial vorticity profile that resembles the Rankine vortex,

$$P(r^*) = \begin{cases} 1 - \exp \left[ -\frac{30}{r^*} \exp \left( \frac{1}{r^* - 1} \right) \right], & \text{if } r^* < 1, \\ 0 & \text{otherwise,} \end{cases} \quad (10)$$

where

$$r^* = \left[ \left( \frac{x - x_0}{a} \right)^2 + \left( \frac{y - y_0}{b} \right)^2 \right]^{1/2} \quad (11)$$

is a nondimensional distance in the radial direction,  $x_0$  and  $y_0$  are the center of the vortex, and  $a$  and  $b$  are the lengths of the major and minor axes, respectively.

The elliptical Rankine-like vortex in the horizontal plane is specified according to

$$\zeta(r^*) = \zeta_0 P(r^*). \quad (12)$$

**Table 1.** The List of Experiments and Parameters

Experiment	$\zeta_0$ ( $s^{-1}$ )	$a$ (km)	$b$ (km)	Structure
WN0	$3 \times 10^{-3}$	24.5	24.5	Circle
WN2-1	$3 \times 10^{-3}$	30.0	20.0	Ellipse
WN2-1S	$6 \times 10^{-3}$	30.0	20.0	Ellipse
WN2-2	$3 \times 10^{-3}$	40.0	15.0	Ellipse
WN2-3	$3 \times 10^{-3}$	60.0	10.0	Ellipse
WN3	$3 \times 10^{-3}$	24.5	24.5	Triangle
WN4	$3 \times 10^{-3}$	24.5	24.5	Square
WN5	$3 \times 10^{-3}$	24.5	24.5	Pentagon

A fixed vorticity of  $\zeta_0 = 3 \times 10^{-3} s^{-1}$  is used in most of our experiments. With the typical vortex size in Table 1, the vortex has a maximum tangential wind of approximately  $30 m s^{-1}$ . The EX-WN0 is a circular vortex with a 24.5 km radius. EX-WN2-1, EX-WN2-2, and EX-WN2-3 are elliptical vortices with aspect ratio of 1.5, 2.7, and 6, respectively, between  $a$  and  $b$ . To study the BL pumping in a stronger vortex, we doubled the vorticity to  $6 \times 10^{-3} s^{-1}$  in experiment EX-WN2-1S.

In experiments with triangular, square, and pentagonal vortex structures, a wave perturbation in the azimuthal direction is added to the specification of  $r^*$  to create the polygonal vortex structure. In such a case the nondimensional distance  $r^*$  is computed by  $a=b=24.5$  km in equation (11). The vorticity field can be expressed as

$$\zeta(\theta, r^*, n) = \zeta_0 P(r_n^*), \quad (13)$$

where

$$r_n^*(\theta) = r^* \times [1 - 0.3 \sin(n\theta)]. \quad (14)$$

For  $n=3$  in equation (13), a triangular eyewall case is produced (EX-WN3), for  $n=4$  a square eyewall case (EX-WN4), and for  $n=5$  a pentagonal eyewall case (EX-WN5). All experiments have initial conditions with different constants  $a$  and  $b$  but under the constraint that the total circulation is conserved for a fixed  $\zeta_0$ . The experiments and the parameters are listed in Table 1.

### 3. Numerical Results

Our first two experiments are similar to those in Kuo *et al.* [1999], with a circular vortex (EX-WN0) and an elliptical vortex (EX-WN2-1) in the free atmosphere. While the tangential wind jet for the free atmosphere is symmetric in the circular vortex, the elliptic vortex has a maximum in the region of minor axis, where the vortex is narrowest due to the conservation of angular momentum (Figure 2). The salient feature in the elliptic vortex is in the BL. The time evolution of the elliptic vortex in the BL from 576 min to

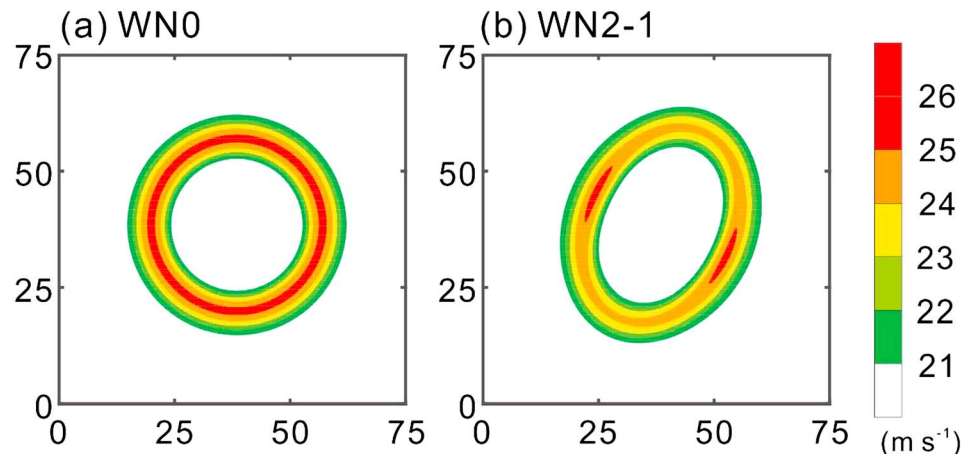


**Figure 2.** Tangential wind in the free atmosphere for the (a) circular vortex (EX-WN0) and (b) the elliptical vortex (EX-WN2-1) experiments at  $t = 720$  min.



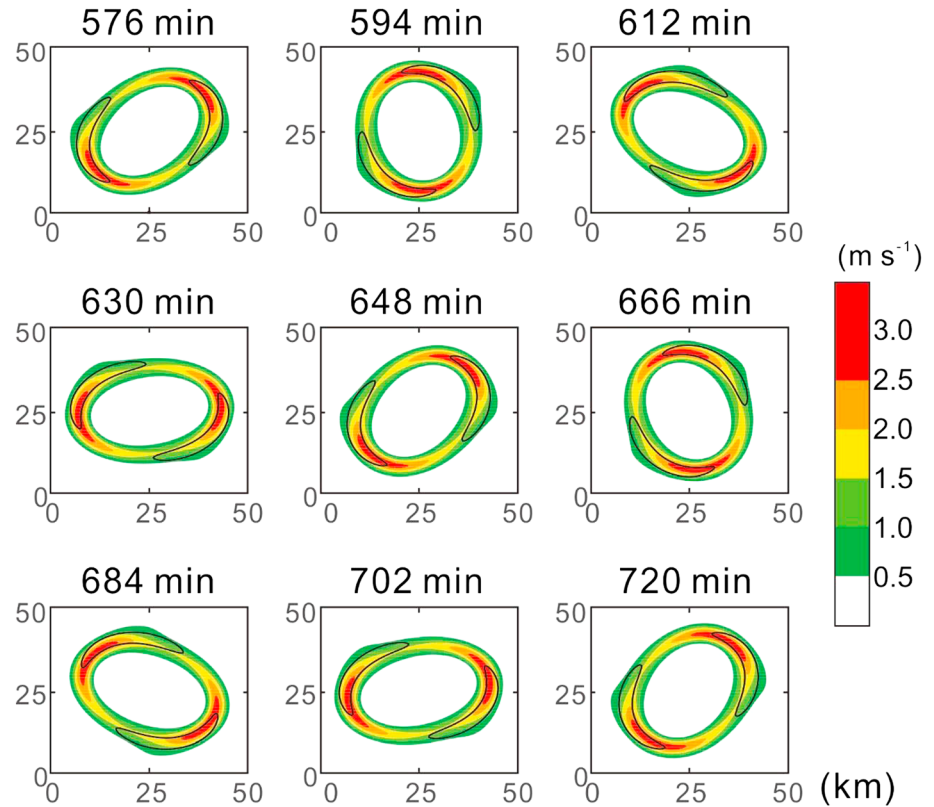


**Figure 3.** Boundary layer updraft (shading) and  $25 \text{ m s}^{-1}$  tangential wind (contour) from 576 min to 720 min of simulation in elliptical vortex experiment (EX-WN2-1).

720 min for a complete rotation of 144 min is shown in Figure 3. Figure 3 depicts the cyclonic rotation of the local high-speed tangential wind and the BL updraft at both sides of the edge of the major axis in the elliptical vortex. The BL updraft has its maximum located on both sides of the edge of the major rotating axis, consistent with the common observation illustrated in Figure 1. This is a result of the pressure gradient force from the free atmosphere represented by the NBM. In Figure 4a, the pressure field for the circular vortex is symmetric and the induced radial wind in the BL is also symmetric. On the other hand, the pressure fields in the elliptic vortex conform to the elliptic structure of the vortex near the core ring but remain circular in the outer area (Figure 4b). This distribution induces larger radial inflow from the pressure gradient force near the edge of the major axis near the core and smaller elsewhere. The dynamic forcing from the free atmosphere thus further induces BL pumping and larger updrafts at the edge of the major axis. The maximum BL updraft at the edge of the major axis is approximately  $3 \text{ m s}^{-1}$  in the elliptic vortex, which is slightly larger than that in the circular vortex.

Figure 5 from the EX-WN2-1 experiment indicates that in the free atmosphere of the elliptic vortex, the tangential wind maximum is located at the smallest vortex ring distance (the minor axis perpendicular to the major axis) from the center (Figure 5a). In the BL, this wind maximum is pushed downstream and closer to the major axis (Figure 5b). Consider the tangential momentum equation without the pressure gradient force in the polar coordinate  $(r, \phi)$ , where  $r$  is the radius and  $\phi$  is the azimuthal angle with radial flow ( $u_r$ ) and tangential flow ( $v_\phi$ ):

$$\frac{Dv_\phi}{Dt} = -\left(\frac{v_\phi}{r} + f\right)u_r.$$

Note from Figure 4b that the radial inflow is largest at the edges of the major axis (negative  $u_r$ ) for the elliptic vortex, so  $Dv_\phi/Dt$  is also the largest. The increase of  $Dv_\phi/Dt$  ahead of the jet maximum pushes it downstream from the minor axis toward the edge of the major axis. The large radial inflow maintains the supergradient wind at the edge of the elliptical vortex. The same mechanism applies to vortices with higher polygonal structures, as will be demonstrated later.

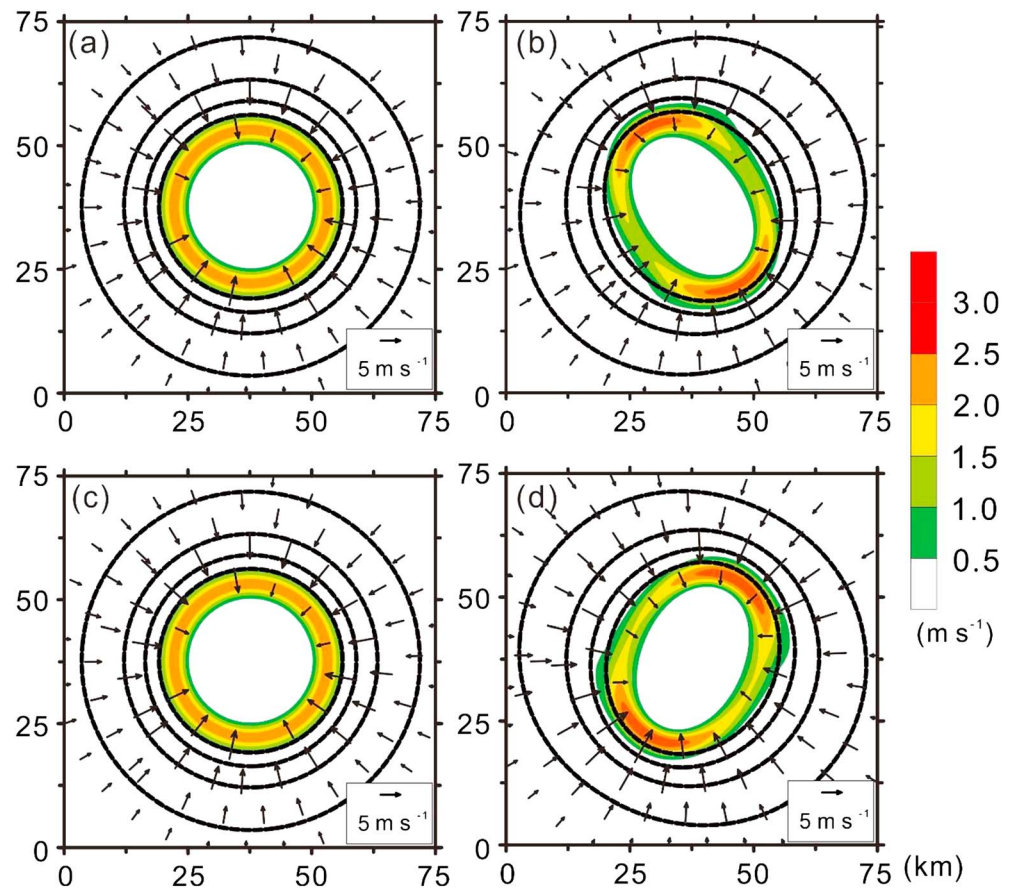


**Figure 4.** The pressure fields in the barotropic model and the updraft, tangential wind, and convergent wind in the slab-boundary layer model for the (a) circular (EX-WN0) and (b) elliptical (EX-WN2-1) vortex experiments at  $t = 360$  min. The black dashed contours are the isobars, with contour levels  $-6$ ,  $-7$ ,  $-8$ , and  $-9$  hPa; the shading is the boundary layer updraft ( $\text{m s}^{-1}$ ); and the black arrow is the convergent wind with magnitude greater than  $3 \text{ m s}^{-1}$ . (c and d) The same as in Figures 4a and 4b except at  $t = 720$  min.

The tangential wind maxima in the SBL model tend to be shifted approximately 5 km inward from the local RMW of the free atmosphere due to BL contraction by the frictional effect. The magnitude of the tangential wind maximum is slightly larger in the SBL than that in the free atmosphere. Discussions of the effect of friction on the inward displacement of the RMW within the BL can be found in *Powell et al.* [2009] and *Keprt* [2001]. The radial profiles of tangential wind, radial wind, and resultant updraft in EX-WN0 and along the major axis of EX-WN2-1 are shown in Figure 6. Figure 6 indicates the existence of supergradient (subgradient) winds inside (outside) the local RMW in both experiments. In general, the supergradient wind is maintained by the large radial inflow. The BL inflow decreases from approximately  $8 \text{ m s}^{-1}$  to zero near the RMW over a radial distance of 6 km for both experiments. This radial inflow profile indicates a shock-like structure in the BL. The upward motion is due to the large deceleration of the radial inflow. Frictional forces are large in the BL; the radial flows caused by the supergradient and the subgradient winds are probably small in comparison.

Additional elliptical vortex experiments with different aspect ratios (EX-WN2-2 and EX-WN2-3), such that the vortex is more elongated, show similar strong updrafts at the edges of the major axis (Figure 7). There are spiral structures emanating out of the updraft from the edges of the major axis due to a wave-breaking effect [Guinn and Schubert, 1993]. The elongated vortices bear similar structures to those observed for Typhoon Herb (Figure 1) at some time frames, such as at 1844 local civil time (LCT) and 1902 LCT on 31 July 1996. The azimuthal-time Hovmöller diagrams of the BL updraft and irrotational wind at a radius of 20 km from the elliptical vortex with different aspect ratios are shown in Figure 8. This figure indicates a general feature of cyclonic rotation of the BL top updraft. The rotation periods of EX-WN2-2

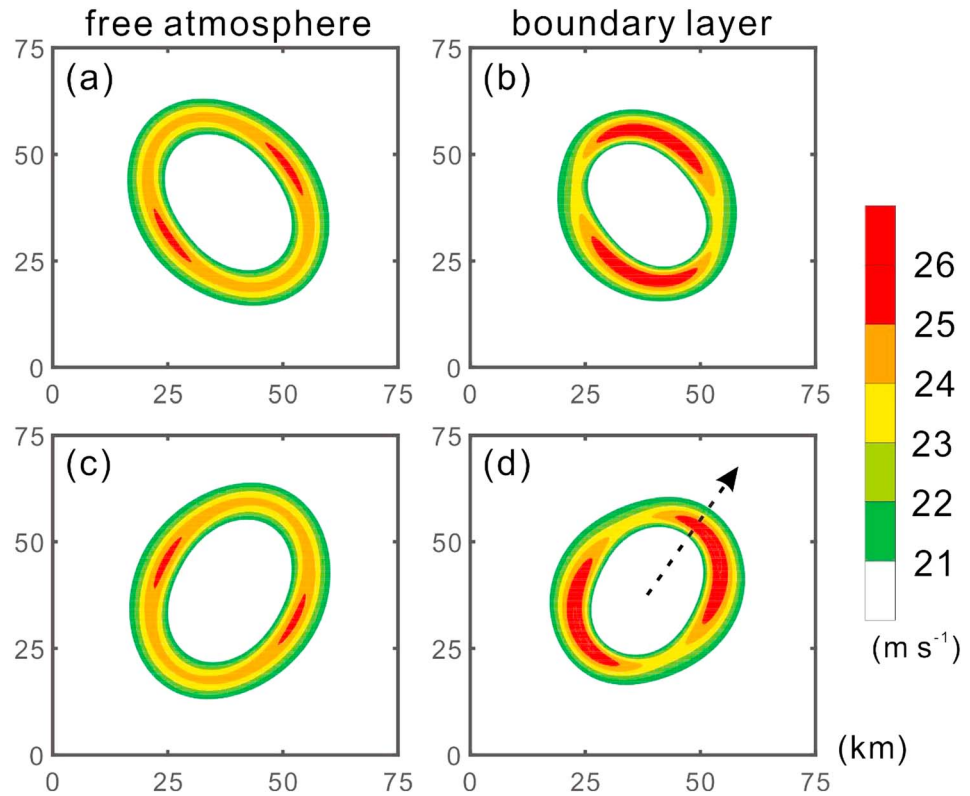


**Figure 5.** Tangential wind field of elliptical vortex experiment (EX-WN2-1) in the (a) free atmosphere and (b) boundary layer at  $t = 360$  min. (c and d) The same as in Figures 5a and 5b but at  $t = 720$  min. The dashed arrow in Figure 5d indicates the orientation of the major axis with the wind shown in profile in Figure 6b.

and EX-WN2-3 are approximately 160 min and 180 min, respectively (Figure 8). For an elliptical vortex with vorticity  $\zeta$  and value of the major axis  $a$  and value of minor axis  $b$ , the rotation period of the Kirchhoff vortex [Lamb, 1932, p. 232] is

$$P = \frac{2\pi (a+b)^2}{\zeta ab}. \quad (15)$$

At 540 min,  $a$  and  $b$  are 26 km and 12 km in the EX-WN2-2 and 25 km and 9 km in the EX-WN2-3, respectively. With a vorticity of  $\zeta_0 = 3 \times 10^{-3} \text{ s}^{-1}$ , the rotation periods of EX-WN2-2 and EX-WN2-3 from the Kirchhoff theory are 161 min and 179 min, respectively. The rotation periods of EX-WN2-2 and EX-WN2-3 from the model are approximately 160 min and 180 min, respectively. The rotation periods of EX-WN2-2 and EX-WN2-3 are generally in agreement with the theory of Kirchhoff elliptical vortex.

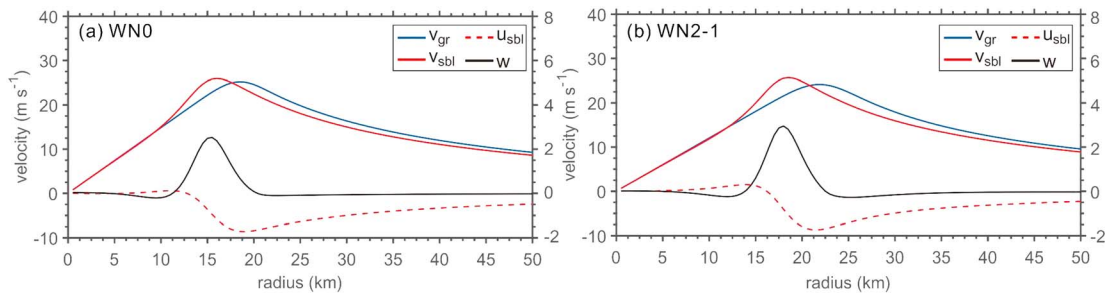


**Figure 6.** Wind profile in (a) the circular vortex experiment (EX-WN0) and (b) along the major axis in the elliptical vortex experiment (EX-WN2-1) at  $t = 720$  min. The blue and red solid curves show the tangential wind in the barotropic model and the slab-boundary layer model. The red dashed line shows the radial wind in slab-boundary layer model. The black solid line shows the boundary layer updraft (right coordinate). The orientation of the wind profile is shown in Figure 5d.



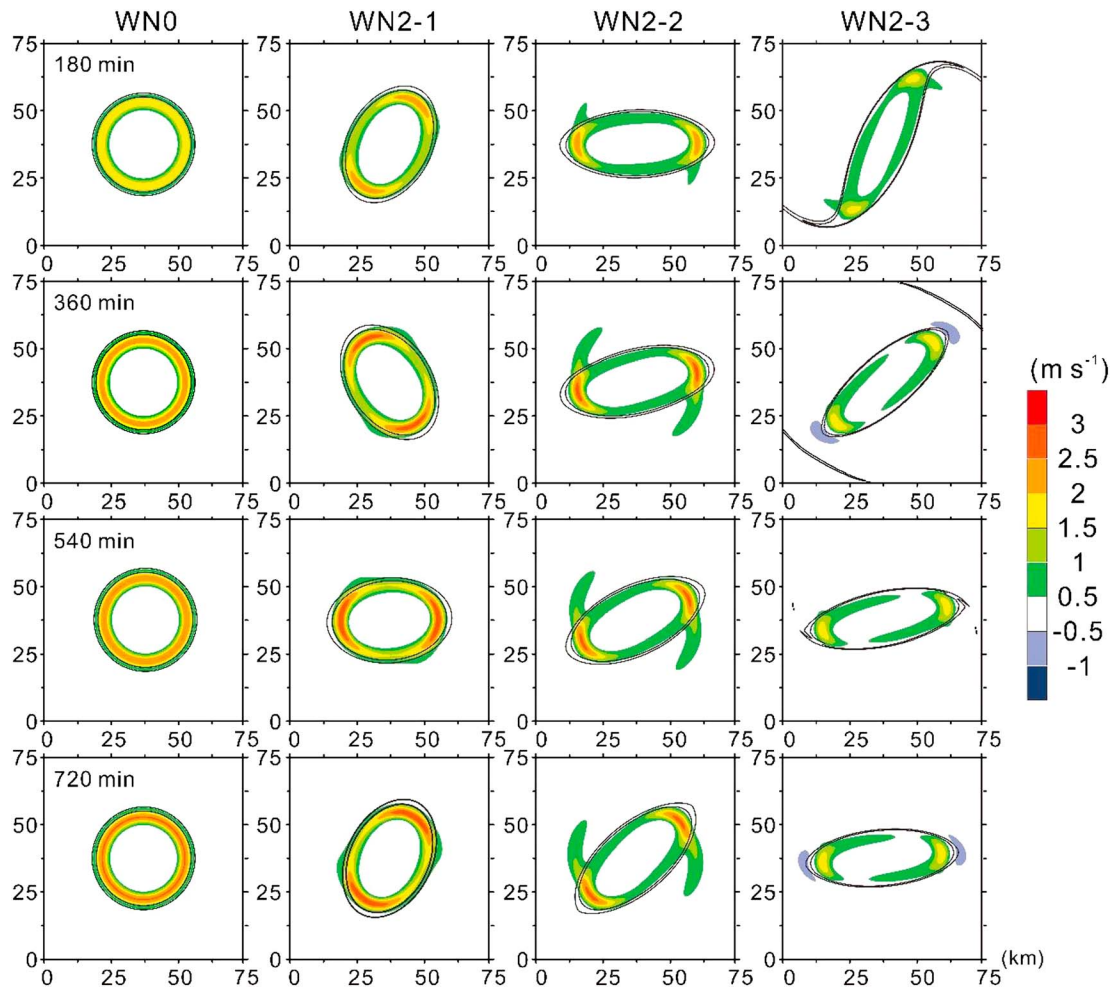


**Figure 7.** Free atmosphere vorticity (black contour levels are  $1 \times 10^{-3}$  and  $2 \times 10^{-3} \text{ s}^{-1}$ ) and boundary layer updraft (shading;  $\text{m s}^{-1}$ ) of the circular and elliptical vortex experiments (EX-WN0, EX-WN2-1, EX-WN2-2, and EX-WN2-3) at  $t = 180, 360, 540$ , and  $720$  min. Each figure shows only the central  $75 \text{ km} \times 75 \text{ km}$  domain.

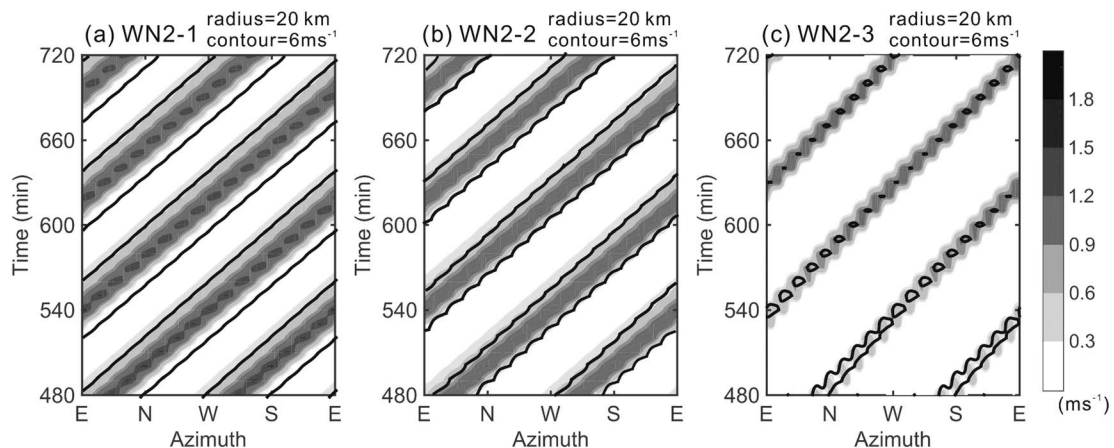


**Figure 8.** Azimuth-time Hovmöller diagram of updraft (shading) and irrotational wind (contour) at radius of 20 km from the vortex center between 480 and 720 min in (a) EX-WN2-1, (b) EX-WN2-2, and (c) EX-WN2-3.

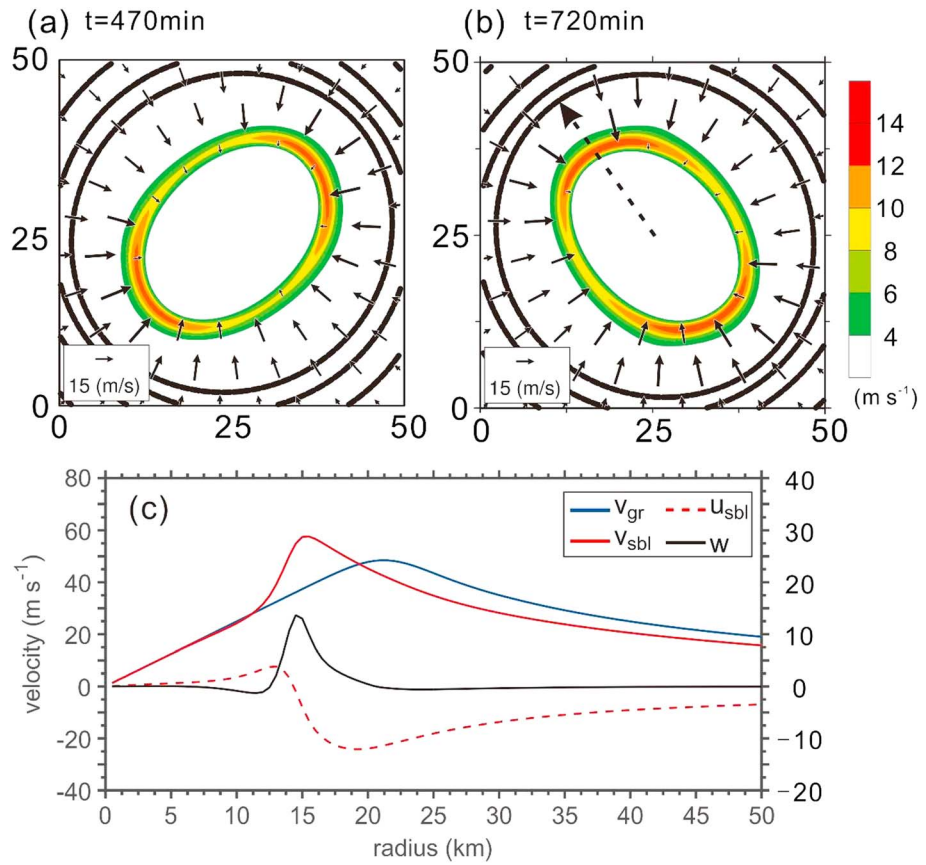


**Figure 9.** Same as in Figure 4 except for the stronger vortex with  $\zeta_0 = 6 \times 10^{-3} \text{ s}^{-1}$  (EX-WN2-15) at (a)  $t = 470$  min and (b)  $t = 720$  min. (c) Same as in Figure 6 except the stronger vortex with  $\zeta_0 = 6 \times 10^{-3} \text{ s}^{-1}$  at  $t = 720$  min. The dashed arrow in Figure 9b indicates the orientation of the wind profile in Figure 9c.

The radial profiles of tangential wind, radial wind, and resultant updraft along the major axis in EX-WN2-2 and EX-WN2-3 are similar to those of EX-WN2-1 in Figure 6 (not shown). The magnitudes of peak tangential wind, radial wind, and updraft decrease with increasing radius of the major axis (Figures 7 and 8). The inertial stability at the major axis of the vortex decreases with radial distance, with those for EX-WN2-2 and EX-WN2-3 smaller than that in EX-WN2-1. As a result, the BL updraft decreases with increasing radius of the major axis.

To further explore the BL pumping in a stronger elliptical vortex, we assign a larger vorticity of  $\zeta_0 = 6 \times 10^{-3} \text{ s}^{-1}$  for experiment EX-WN2-15 (Figure 9). Larger radial inflow is induced by the pressure

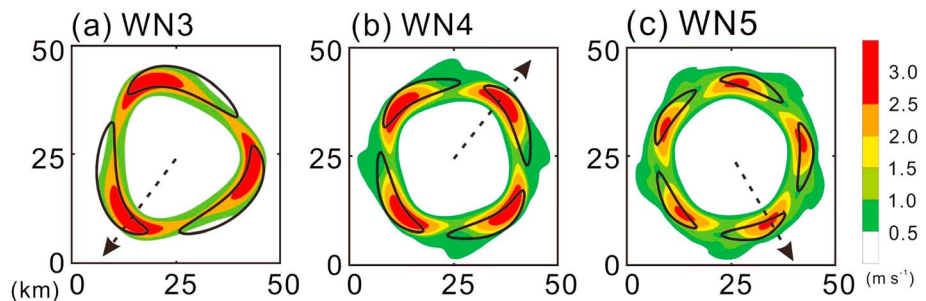


**Figure 10.** Boundary layer updraft (shading) and 25  $\text{m s}^{-1}$  tangential wind (contour) of the (a) triangular, (b) square, and (c) pentagonal vortices (EX-WN3, EX-WN4, and EX-WN5) at  $t = 720$  min. The dashed arrows indicate the orientations of the major axis with the wind shown in profile in Figure 12.

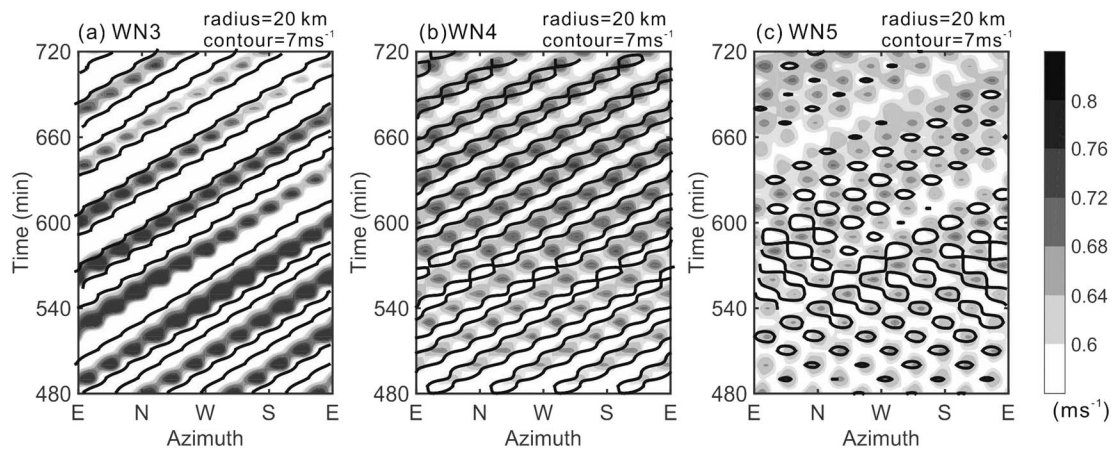


**Figure 11.** Same as in Figure 8 except for the (a) triangular, (b) square, and (c) pentagonal vortices (EX-WN3, EX-WN4, and EX-WN5).

gradient force near the edge of the major axis and smaller elsewhere. The BL pumping occurs at the edges of the major axis as in EX-WN2-1. The BL inflow near RMW decreases from approximately  $24 \text{ m s}^{-1}$  to zero over a radial distance of 4 km. The BL updraft in EX-WN2-1S is sharper in the horizontal structure compared to EX-WN2-1. The updraft magnitude is approximately  $13 \text{ m s}^{-1}$ , which is about 5 times greater. This much stronger updraft is similar to the shock-like radial profile of the symmetric vortex in Williams *et al.* [2013].

As discussed by Kepert [2010a] and Abarca *et al.* [2015], the use of a SBL model in TC simulations can cause excessively strong inflow and too large of a departure from gradient wind balance. By mass continuity, this can manifest updrafts at the top of the BL that are stronger than those obtained with a height-resolving BL model. The agreement of our results with observations on the maximum updraft at the edges of the major axis in BL and the rotation of the updraft indicate the applicability of our model for the understanding of associated dynamics.

To further investigate the BL pumping in polygonal vortices, we conduct triangular vortex, square vortex, and pentagonal vortex experiments (EX-WN3, EX-WN4, and EX-WN5). As in the elliptical vortex experiment of Figure 3, the BL local maximum of tangential wind and stronger BL updrafts occurred at the edges of the polygonal vortices (Figure 10). It is evident that, with the same vorticity strength in the polygonal vortices, the magnitude of the peak updraft is decreasing with increasing wave number of the vortex. For example, the maximum updrafts for the elliptical, triangle, quadrangle, and pentagonal vortices are  $3.0 \text{ m s}^{-1}$ ,  $2.8 \text{ m s}^{-1}$ ,  $2.2 \text{ m s}^{-1}$ , and  $1.9 \text{ m s}^{-1}$ , respectively, for the control vorticity of  $\zeta_0 = 3 \times 10^{-3} \text{ s}^{-1}$ . We also use a stronger vorticity of  $\zeta_0 = 6 \times 10^{-3} \text{ s}^{-1}$ ; the maximum SBL updrafts of the elliptical, triangle, quadrangle, and pentagonal vortices are  $13 \text{ m s}^{-1}$ ,  $12.3 \text{ m s}^{-1}$ ,  $10.8 \text{ m s}^{-1}$ , and  $10.1 \text{ m s}^{-1}$ , respectively (not shown). The azimuthal-time Hovmöller diagrams of the BL updraft and irrotational wind in EX-WN3, EX-WN4, and EX-WN5 show that the periods of cyclonic rotation are approximately 104, 93, and 87 min, respectively (Figure 11). The cyclonic periods also are in general agreement with the linear theory of Kelvin [Thomson, 1880]. The radial profiles of supergradient wind, subgradient wind, radial wind, and updraft at the edges of

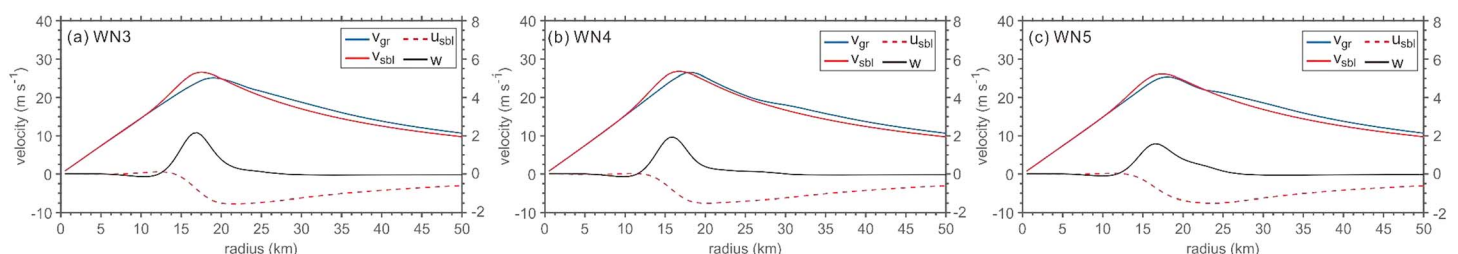


**Figure 12.** Same as in Figure 6 except for the (a) triangular, (b) square, and (c) pentagonal (EX-WN3, EX-WN4, and EX-WN5) vortices at  $t = 720 \text{ min}$ . The orientations of wind profiles are shown in Figure 10.

the polygonal vortices are shown in Figure 12. The results are similar to that of the elliptical vortex in Figure 6. The profile is a robust feature of the BL response to the polygonal vortices, which is similar to Figure 4 of Shapiro [1983] for the aircraft observations in Hurricane Hugo (1989) and radar reflectivity patterns in Hurricane Dolly (2008) [Hendricks *et al.*, 2012, Figure 4]. Because the rotation of the polygonal vortex is due to the nondivergent VRW [Kuo *et al.*, 1999], our results support the notion of the nondivergent VRWs organize the BL winds and convection in the polygonal eyewalls of TC.

#### 4. Summary and Concluding Remarks

There are many observations indicating that deep convection often occurs near the edges of the major axis of elliptical eyewall and rotates cyclonically. We use a nondivergent barotropic model (NBM) combined with an asymmetric slab boundary layer (SBL) model to investigate the phenomenon. The NBM allows the simulation of the nonlinear vorticity dynamics of VRWs in the TC-like polygonal vortices, and the asymmetric SBL model allows for the frictional pumping and associated updrafts at the top of the BL. The pressure gradient force in the NBM is in gradient wind balance. In the SBL model, such a balance does not exist due to frictional effects and radial inflow is generated by the imposed pressure gradient force. The interaction is one way in our calculation; the NBM provides time-varying pressure gradient forcing to drive the SBL model below. However, the SBL model does not feed back to the NBM. The BL flow driven by the time-varying pressure field is divergent so that the spatial distribution of BL pumping (updraft on top of BL) can be calculated. The strong updrafts (and convergence) at the edges of the major axis for the elliptical vortex in the BL are induced by the larger convergent radial wind from the asymmetric distribution of the pressure fields of the free atmosphere with a noncircular vortex. The large radial inflow maintains the supergradient wind at the edge of the major axis for the elliptical vortex. Similar radial profiles and strong BL top updrafts occur at the edges of higher-order polygonal eyewalls. In general agreement with observations, the results emphasize the cyclonic rotation of strong updrafts at top of the BL at the edges of polygonal eyewalls.

Our simple model approach does not allow the divergent effect in the free atmosphere. Shapiro and Montgomery [1993] and Montgomery and Franklin [1998] have argued and demonstrated that the magnitude of the asymmetric divergence at the top and above the TC BL is of the same order as the asymmetric vertical relative vorticity and cannot be neglected. Wang [2002] indicated that the BL pumping occurred in the azimuthal direction at about one-quarter wavelength farther downstream from the edges of the major axis of elliptical eyewalls due to the divergence at top of the BL. The divergence appears to be associated with positive vorticity advection from the cyclonic rotation of elliptical vortex. The BL pumping occurring downstream from the edges of the major axis of elliptical eyewalls does not seem to be consistent with the observations. While a SBL model combined with a shallow water model may better represent the divergent forcing, our NBM may be the simplest approach to the problem within the hierarchy models without divergent forcing.

In the radial flight leg observation of Hurricane Hugo (1989), the BL inflow decreased from approximately  $22 \text{ m s}^{-1}$  to zero over a radial distance of a few kilometers and an updraft of  $22 \text{ m s}^{-1}$  was observed [Williams *et al.*, 2013]. Williams *et al.* [2013] used an axisymmetric SBL model to interpret the observation as a shock-like structure in BL radial inflow. Shapiro [1983] studied WN1 BL structures in a translating TC. The radial wind profile in his result showed the supergradient (subgradient) wind inside (outside) the local radius of maximum wind in the BL, in general agreement with that of Hurricane Hugo except that the simulated updraft is only around  $3 \text{ m s}^{-1}$ . With a vorticity of  $6 \times 10^{-3} \text{ s}^{-1}$  in our experiments, the updraft is in the order of  $13 \text{ m s}^{-1}$  at the edges of the polygonal eyewalls, similar to the observations reported in Shapiro [1983] and Williams *et al.* [2015]. An estimate of the updraft from the Ekman pumping [Kepert, 2010a, 2010b, 2013] around the eyewall from the EX-WN2-1S is about  $0.3 \text{ m s}^{-1}$ , which is much smaller than the updrafts in Shapiro [1983], Williams *et al.* [2013], and in our model. Our model simulation for the BL inflow decreases from approximately  $24 \text{ m s}^{-1}$  to zero over a short radial distance of 4 km at the edge of the major axis of elliptical vortex. The shock-like local radial profile of winds and strong updraft may be a ubiquitous BL feature of TCs. Such local radial profiles of BL winds may be an essential ingredient of a TC vortex with a well-defined symmetric or asymmetric updraft structure around the eyewall. With simple dynamical model calculations, our intent is not to undermine the importance of the full physics model but rather to isolate the fundamental dynamics that may be responsible for this phenomenon. Careful analysis of real-case TC BL data as well as fine-scale simulations of the BL in full physics models will be the future work.



## Acknowledgments

The authors would like to thank the anonymous reviewers, Mr. Paul Ciesielski, and Prof. Wayne H. Schubert for their insightful comments. The radar data can be obtained from Central Weather Bureau in Taiwan ([https://cwbebox.cwb.gov.tw/ebox\\_formfill/ebox\\_visFormFill.php](https://cwbebox.cwb.gov.tw/ebox_formfill/ebox_visFormFill.php)). This work was supported by Ministry of Science and Technology in Taiwan under grants MOST 104-2111-M-002-002-MY3, MOST 104-2625-M-002-006, and MOST-105-2119-M-002-035 and the Naval Research Laboratory under grant N62909-15-1-2008.

## References

- Abarca, S. F., M. T. Montgomery, and J. C. McWilliams (2015), The azimuthally averaged boundary layer structure of a numerically simulated major hurricane, *J. Adv. Model. Earth Syst.*, *7*, 1207–1219, doi:10.1002/2015MS000457.
- Aberson, S. D., J. P. Dunion, and F. D. Marks Jr. (2006), A photograph of a wavenumber-2 asymmetry in the eye of Hurricane Erin, *J. Atmos. Sci.*, *63*, 387–391.
- Braun, S. A. (2002), A cloud-resolving simulation of Hurricane Bob (1991): Storm structure and eyewall buoyancy, *Mon. Weather Rev.*, *130*, 1573–1592.
- Corbosiero, K. L., J. Molinari, A. R. Aiyyer, and M. L. Black (2006), The structure and evolution of Hurricane Elena (1985). Part II: Convective asymmetries and evidence for vortex Rossby waves, *Mon. Weather Rev.*, *134*, 3073–3091.
- Duchon, C. E. (1979), Lanczos filtering in one and two dimensions, *J. Appl. Meteorol.*, *18*, 1016–1022.
- Guinn, T. A., and W. H. Schubert (1993), Hurricane spiral bands, *J. Atmos. Sci.*, *50*, 3380–3403.
- Hendricks, E. A., B. D. McNoldy, and W. H. Schubert (2012), Observed inner-core structural variability in Hurricane Dolly (2008), *Mon. Weather Rev.*, *140*, 4066–4077.
- Itano, T., and M. Hosoya (2013), Spectral analyses of the polygonal eye of Typhoon Sinlaku, *Mon. Weather Rev.*, *141*, 987–996.
- Kepert, J. D. (2001), The dynamics of boundary layer jets within the tropical cyclone core. Part I: Linear theory, *J. Atmos. Sci.*, *58*, 2469–2484.
- Kepert, J. D. (2010a), Slab- and height-resolving models of the tropical cyclone boundary layer. Part I: Comparing the simulations, *Q. J. R. Meteorol. Soc.*, *136*, 1686–1699.
- Kepert, J. D. (2010b), Slab- and height-resolving models of the tropical cyclone boundary layer. Part II: Why the simulations differ, *Q. J. R. Meteorol. Soc.*, *136*, 1700–1711.
- Kepert, J. D. (2013), How does the boundary layer contribute to eyewall replacement cycles in axisymmetric tropical cyclones?, *J. Atmos. Sci.*, *70*, 2808–2830.
- Kuo, H.-C., and C.-T. Cheng (1999), Experiments with a spectral convection model, *TAO*, *10*, 651–692.
- Kuo, H.-C., R. T. Williams, and J.-H. Chen (1999), A possible mechanism for the eye rotation of Typhoon Herb, *J. Atmos. Sci.*, *56*, 1659–1673.
- Kurihara, Y., and M. A. Bender (1982), Structure and analysis of the eye of a numerically simulated tropical cyclone, *J. Meteorol. Soc. Jpn.*, *60*, 381–395.
- Lamb, H. (1932), *Hydrodynamics*, 6th ed., 732 pp., Dover, New York.
- Mitsuta, Y., and S. Yoshizumi (1973), Periodic variation of pressures, wind and rainfall observed at Miyakojima during the Second Miyakojima Typhoon, *J. Meteorol. Soc. Jpn.*, *51*, 475–485.
- Montgomery, M. T., and J. L. Franklin (1998), An assessment of the balance approximation in hurricanes, *J. Atmos. Sci.*, *55*, 2193–2200.
- Montgomery, M. T., and R. J. Kallenbach (1997), A theory for vortex Rossby-waves and its application to spiral bands and intensity changes in hurricanes, *Q. J. R. Meteorol. Soc.*, *123*, 435–465.
- Muramatsu, T. (1986), The structure of polygonal eye of a typhoon, *J. Meteorol. Soc. Jpn.*, *64*, 913–921.
- Ooyama, K. (1969), Numerical simulation of the life cycle of tropical cyclones, *J. Atmos. Sci.*, *26*, 3–40.
- Powell, M. D. (1982), The transition of the Hurricane Frederic boundary-layer wind field from the open Gulf of Mexico to landfall, *Mon. Weather Rev.*, *110*, 1912–1932.
- Powell, M. D., P. J. Vickery, and T. A. Reinhold (2003), Reduced drag coefficient for high wind speeds in tropical cyclones, *Nature*, *422*, 279–283.
- Powell, M. D., E. W. Uhlhorn, and J. D. Kepert (2009), Estimating maximum surface winds from hurricane reconnaissance measurements, *Weather Forecast.*, *24*, 868–883.
- Shapiro, L. J. (1983), The asymmetric boundary layer flow under a translating hurricane, *J. Atmos. Sci.*, *40*, 1984–1998.
- Shapiro, L. J., and M. T. Montgomery (1993), A three-dimensional balance theory for rapidly rotating vortices, *J. Atmos. Sci.*, *50*, 3322–3335.
- Thomson, W. (1880), Vibrations of a columnar vortex, *Philos. Mag.*, *10*, 155–168.
- Wang, Y. (2002), Vortex Rossby waves in a numerical simulated tropical cyclone. Part I: Overall structure, potential, and kinetic energy budgets, *J. Atmos. Sci.*, *59*, 1213–1238.
- Williams, G. J. (2015), The effects of vortex structure and vortex translation on the tropical cyclone boundary layer wind field, *J. Adv. Model. Earth Syst.*, *7*, 188–214.
- Williams, G. J., R. K. Taft, B. D. McNoldy, and W. H. Schubert (2013), Shock-like structures in the tropical cyclone boundary layer, *J. Adv. Model. Earth Syst.*, *5*, 338–353, doi:10.1002/jame.20028.
- Zhang, J. A., and M. T. Montgomery (2012), Observational estimates of the horizontal eddy diffusivity and mixing length in the low-level region of intense hurricanes, *J. Atmos. Sci.*, *69*, 1306–1316.